Straintronics with single-layer MoS_2: A quantum Monte Carlo study

Y. Huang,[1] M. Manzoor,[2] J. Brndiar,[1] M. Milivojevic,[1,3] and I. Štich[1,2,4,*]

[1]*Institute of Informatics, Slovak Academy of Sciences, 845 07 Bratislava, Slovakia*
[2]*Institute of Physics, Slovak Academy of Sciences, 84511 Bratislava, Slovakia*
[3]*Faculty of Physics, University of Belgrade, 11001 Belgrade, Serbia*
[4]*Department of Natural Sciences, University of Ss. Cyril and Methodius, 917 01 Trnava, Slovakia*

(Received 14 August 2023; revised 9 October 2023; accepted 4 December 2023; published 3 January 2024)

Using state-of-the-art quantum Monte Carlo (QMC) methods, we study straintronic properties of a single MoS_2 monolayer. 2D MoS_2 is a quintessential straintronic material for which many experiments have been performed. First, we determine the equilibrium atomic structure which is not known experimentally and is strictly needed to correctly determine the straintronic properties. That enables us to precisely analyze the quasiparticle band gaps for any applied biaxial strain, which we describe by a bivariate paraboloid function of lattice constant and internal structural parameter. Using the fixed-node QMC calculations fitted by analytical formulas, we localize the following excited state crossings between the direct, $K \rightarrow K$, and indirect $\Gamma \rightarrow X$ and $K \rightarrow K/2$ excitations. Based on this highly accurate many-body treatment, we predict a gauge factor of 136 meV/% for the $K \rightarrow K$ transition and a fairly narrow window of ≈2.8% from compressive to mildly tensile strains, accounting for only ≈0.3 eV band gap change maintaining the direct character of the gap. Consequently, we suggest that, compared to other 2D materials, such as phosphorene, there is only a limited straintronic tuneability in this material often studied for its straintronic properties. QMC results are compared to results of standard DFT modeling, which reveal insights into the corresponding inaccuracies and therefore open a window for educated use of rapid DFT approaches.

DOI: 10.1103/PhysRevResearch.6.013007

I. INTRODUCTION

Two-dimensional (2D) materials have a range of superior electronic, optical, thermal, spin, and magnetic properties [1–7]. In particular, 2D materials usually possess ultrahigh carrier mobility and field-effect switching ratios, which make them ideal materials for field-effect and digital logic transistors [8]. In addition, 2D materials with appropriate and tuneable direct band gap have achieved extremely efficient photon absorption, emission, and photoelectric conversion and have been widely used in the field of optoelectronic devices [9]. To meet more demands, various techniques have been exploited to modulate their properties, including doping, alloying, forming van der Waals heterostructures, and strain engineering [10–12].

One of the most distinguishing properties of 2D materials is their ability to continuously tune their properties. Due to their atomic thickness, 2D materials are highly sensitive to external perturbations, such as strain. Their resilience to mechanical deformations allows application of strains well in excess of 10%. For instance, graphene [13] and MoS_2 [14] have been shown to sustain strains of ≈25% and ≈11%, respectively. By applying strain, the lattice and electronic structure is modulated as well as their various properties. Strain engineering has been recently widely used in the semiconductor industry. For instance, by applying tensile strain in a silicon transistor, the carrier mobility can be greatly enhanced [15]. However, bulk single crystals can only withstand strain of up to ≈2%, largely limiting their strain modulation. This is where 2D materials able to withstand much larger strain loads come to fruition.

Application of strain to 2D materials [10–12], or straintronics, developed as an emerging field enabling unqiue tuneable functionalities. Many straintronic experiments have been performed on 2D MoS_2 [16–20]. These experiments which have applied subpercent mainly uniaxial strains have demonstrated gauge factors in the range of 30–125 meV/% with band gap tuning of a few dozens of meV. In contrast, the study of single-layer phosphorene, using the highly accurate quantum Monte Carlo methods [21] (QMCs), we have predicted that single-layer phosphorene not only exhibits a similar band gap gauge factor to MoS_2 of ≈100 meV/%, but, at the same time, it keeps the direct $\Gamma \rightarrow \Gamma$ nature of the band gap over a very large window of applied strains primarily in the tensile region, thus making tuning of the band gap accessible within several tenths of eV [22].

Our use of the benchmark-quality QMC methods is motivated by our previous results for freestanding single-layer phosphorene [22,23]. The major mainstream methods, such as DFT and *GW*, depending on the approximations used,

*ivan.stich@savba.sk

exhibited spreads of the quasiparticle band gaps of the order of ≈1 eV. Benchmarking of these various results against experimental results is complicated by experimental uncertainties due to impacts from dielectric embedding, capping, presence of defects, and different sensitivities of experimental probes to their presence, leading to a comparable spread of the experimental values of ≈1 eV. Such uncertainty is fairly typical for electronic properties of 2D materials. Therefore, a high-quality many-body calculation is highly desirable for understanding the various factors affecting the results and for opening up a path of educated tuning [22,23]. For instance, the fixed-node QMC value of the quasiparticle gap in equilibrium [22] was within chemical accuracy from the experimental value for freestanding single-layer phosphorene [24] and the straintronic properties are expected to match the same level of accuracy [22].

Motivated by previous success, we have now also applied the QMC methods to a straintronic study of single-layer MoS_2. In particular, a benchmark-quality quasiparticle band gap has been determined for a wide range of applied strain. In addition, we obtained insights into structural parameters in and out of equilibrium at the QMC level and therefore also offer high-quality equilibrium data. We have also determined the boundaries separating the region of the direct K → K transition and the Γ → K (tensile strains) and K → K/2 (compressive strain). Interestingly, while small in absolute value, the spin-orbit couplings (SOCs) have a non-negligible effect on the precise location of the boundaries. Our study revealed a high value of gauge factor but, surprisingly, only a fairly limited range of strains (≈2.8%) from compressive to mildly tensile, accounting for only ≈0.3 eV band gap change, maintaining the direct character of the gap. However, as for the more important tensile strain, at variance with phosphorene where most of the direct band gap tuning is in the tensile region by many percent, MoS_2 can only sustain ≈0.5% bidirectional tensile strain before the band gap changes from direct K → K to indirect Γ → K. As a natural reference, these results for the quintessential straintronic MoS_2 material are compared with results for freestanding phosphorene obtained with the same benchmark fixed-node QMC methods [22]. Several DFT [25–27] and even *GW* [28] straintronic studies have been previously published. Hence, for the purpose of methods benchmarking, our QMC results are compared with results of the ubiquitous DFT methods in commonly used approximations (GGA, hybrids) so as to offer insights into their biases.

II. COMPUTATIONAL METHODS

The electronic quasiparticle band gap, Δ_f, in monolayer MoS_2, for structure, see Fig. 1, is calculated as singlet-singlet vertical excitation energy,

$$\Delta_f \approx E_v^{ss} = E_1^s - E_0^s \quad , \tag{1}$$

with E_0 and E_1 being the ground and first excited states. The neutral gap defined by Eq. (1) under present conditions corresponds to the fundamental gap [29]. We use periodic boundary conditions where E_0 and E_1 were computed by the diffusion Monte Carlo method in fixed-node approximation using variational Monte Carlo trial wave functions with the

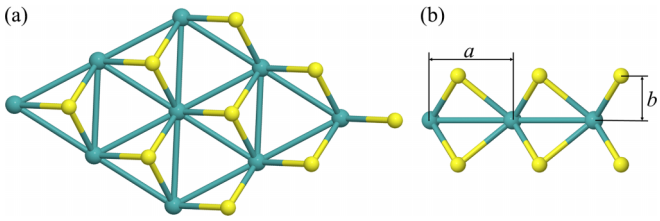

FIG. 1. Structure and basic structural parameters of the monolayer MoS_2. (a) Top view of the structure. (b) Side view with the basic structural parameters: a, the lattice parameter, and the internal structural parameter b.

nodal hypersurfaces determined by DFT orbitals using the generalized gradient approximation DFT-PBE [30] at the Γ point of the Brillouin zone, with short-range correlations described by the Jastrow factor [21]. The DFT calculations were also performed in hybrid DFT-HSE [31] and DFT-B3LYP [32] models. The rational for selecting the DFT-PBE exchange-correlation functional for fixing the nodal hypersurfaces is motivated by its ability to describe the equilibrium properties, deformation energies, and boundaries between different excitations in fairly good agreement with the fixed-node QMC results.

Of key importance is finite-size scaling of each excitation considered. Finite-size scaling was performed for a series of periodic supercells, see Fig. 2, with $N/N_e = 9/234$, $12/312$, and $15/390$ primitive unit cells and number of electrons for K → K and Γ → K transitions and with $12/312$ and $18/468$ supercells for the K → K/2 transition, using linear scaling with $1/N$ [23]. As shown in Fig. 3 for K → K and Γ → K transitions, the 9, 12, and 15 approximants provide a well converged solution. Contrary, the K → K/2 transition is much more difficult to converge and larger approximants, namely, 12 and 18, had to be used. The structural parameters a and b for the largest approximants used for the finite-size scaling appear to be well converged as well [33]. The finite-size scaling is statistically converged to within the chemical accuracy.

Experimentally, the strain can be applied either uniaxially or biaxially. Since experimental application of biaxial strain leads to a gauge factor more than twice larger than application

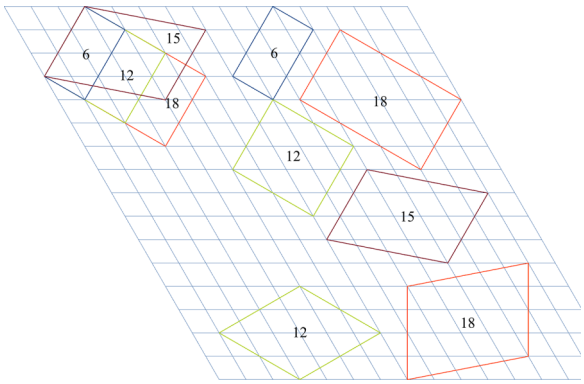

FIG. 2. Structural approximants. Various structural supercells sizes considered for selection of finite-size scaling. Supercells containing 9, 12, 15, and 18 primitive unit cells were used in present calculations.

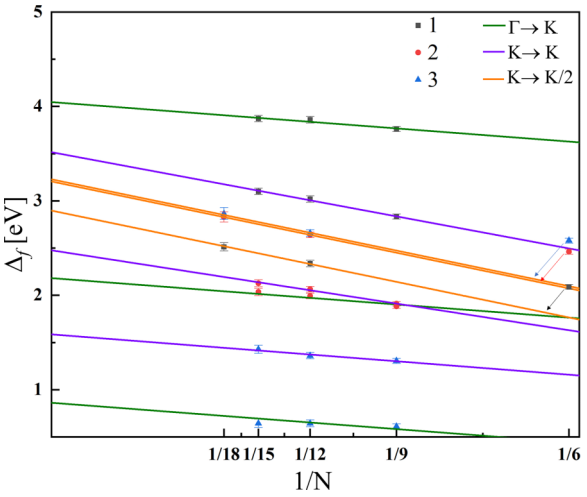

FIG. 3. Finite-size scaling for all three points, see the inset, used in the parabolic approximation for the K → K, Γ→K, and K→K/2 transitions.

of uniaxial strain and the higher symmetry of the problem reduces significantly the computational cost, we have studied only the effect of biaxial strain. The strain was applied in a diagonal direction by adjusting the lattice parameter a, see Fig. 1, considering deformations of up to ≈±10% both compressive and tensile. In determination of strained properties, we follow the procedure recently developed for straintronic study of phosphorene [22], namely, by treating them as a full optimization problem in the space of two structural variables: lattice parameter a and one internal parameter b, see Fig. 1. Around the minima, the data for E_0 were fitted by 2D paraboloid functions used to find the lowest point on the b subspace, leaving us to further deal with only single-variate functions, $E_0 = f(a)$. The excited state E_1 is computed only at the minimum for the internal parameter b. By comparison, in phosphorene [22] the optimalization is more complex, as there we deal with optimization in 4D space (two lattice parameters a, b and two internal coordinates x and y).

As known experimentally [34], 2D MoS_2 exhibits pronounced SOC effects. However, our energy scale is dictated by the straintronic effect and on that energy scale the SOC effects are non-negligible but fairly small. Therefore, rather than sampling them via QMC [35], we have applied them perturbatively via DFT-PBE modeling on top of our QMC results. For more details, see Appendix C.

QMC calculations were performed with the QMCPACK suite of codes [36]. All DFT calculations, including the SOC effects, were done with the QUANTUM ESPRESSO package [37]. For more technical details, see Ref. [33].

III. RESULTS AND DISCUSSION

A. Quasiparticle band gap

To set the stage, we first scanned the band gap response to strain by DFT-PBE techniques [33]. In equilibrium, the band gap in single-layer MoS_2 is direct at K [16]. Application of strain, in general, modifies the nature of the band gap and other gap types corresponding to different transitions occur

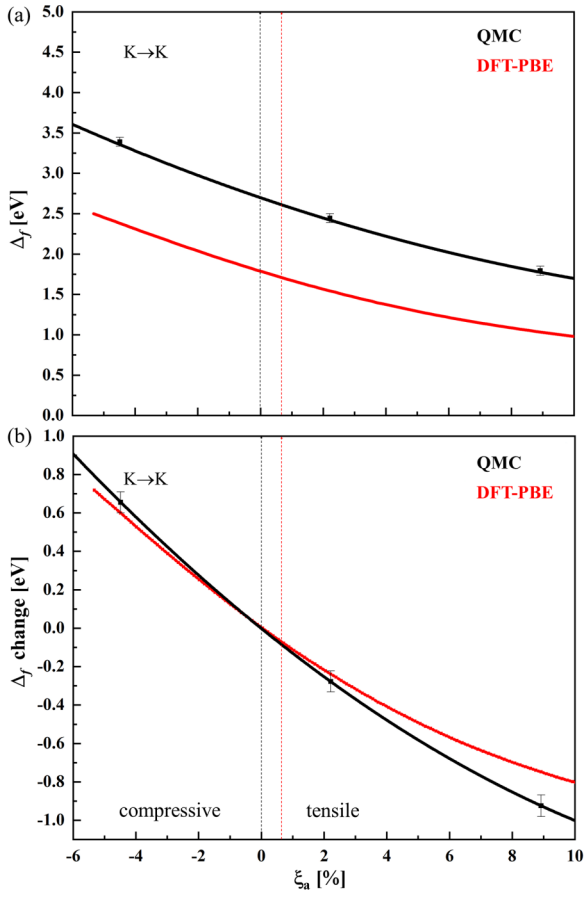

FIG. 4. Fundamental gap as a function of applied strain. (a) Fundamental gap, Δ_f, for the K → K transition as calculated in fixed-node QMC and in DFT-PBE treatment. (b) Change of Δ_f by applied diagonal strain with respect to the equilibrium Δ_f within each approach. Zero strain corresponds to the fixed-node QMC value; the respective fixed-node QMC and DFT-PBE equilibrium values are indicated by black and red vertical dashed lines.

[33]. Accordingly, we have first selected our QMC calculations to be confined primarily to the K → K region of the band gap, i.e., close to the equilibrium and, then again, using the fixed-node QMC, and determined the boundaries of the direct K → K transition and the K → K/2, corresponding to compressive strains, and to Γ → K corresponding to tensile strains. The procedures used here are scaled down from the 4D to 2D procedures we developed for straintronic study of phosphorene [22].

The fixed-node QMC fundamental (quasiparticle) gap at the K point as a function of applied strain is shown in Fig. 4(a); parameters of the paraboloid fit can be found in Appendix B. In Fig. 4, the fixed-node QMC result is compared to DFT-PBE, which was used to fix the nodal hypersurfaces. Results of the other DFT models shown in Appendixes A–C indicate that DFT-PBE gives results overall in best agreement with the fixed-node QMC.

The trends in both QMC and DFT-PBE are qualitatively similar; compressive strain increases the gap whereas tensile strain diminishes it. Note that the QMC and DFT-PBE curves are essentially parallel, the main difference between

the QMC and DFT descriptions being the band gap reduction by ≈1 eV in the DFT-PBE description and a shift of the DFT-PBE minimum by about +0.76%, see also Sec. III C below. For our QMC optimized *structure at equilibrium* we obtain $a = 3.159 \pm 0.0006$ Å, $b = 1.577 \pm 1.2\text{e-}5$ Å, and $\Delta_f = 2.69 \pm 0.051$ eV. The DFT-PBE results are $a = 3.180$ Å, $b = 1.566$ Å, and $\Delta_f = 1.69$ eV. These QMC results are a valuable reference as the structural properties of 2D materials may, in principle, be heavily influenced by substrates which typically provide unintentional property tuning of both electronic and structural properties in experiments. However, this tuning of structural properties is fairly minute in MoS_2. To provide a quantitative measure for the effect, we provide a comparison with the 3D 2H-MoS_2 crystal: $a = 3.160$ Å, $b = 1.586$ Å. Clearly, in this system where the layers are purely vdW bonded, the effect on the structural parameters is very limited. This is at variance with single-layer phosphorene where, presumably due to at least a partial interlayer chemical bonding, the structural parameters are fairly strongly affected by the substrates [22]. The small differences in structural properties between fixed-node QMC and experiment on 3D crystal is likely due to the weak vdW interlayer interaction, the difference between fixed-node QMC and DFT-PBE is more likely caused by the +0.76% difference in the equilibrium lattice constant; see also Sec. III C. More difficult is the comparison of the quasiparticle band gaps with experiments. For instance, a single-layer MoS_2 band gap can be modulated from 2.8 eV to 1.9 eV by dielectric environment [38] which, as discussed above, had negligible effect on the structural properties due to the pure vdW interaction with the substrates. Comparison of fixed-node QMC equilibrium properties with hybrid functionals and many-body perturbation theory within *GW* approximation (*GW*) is compiled in Appendix A. DFT-HSE provides the best lattice parameter and the DFT-B3LYP the best band gap albeit the least accurate lattice parameter. Comparison with the *GW* shows fairly good agreement of the quasiparticle band gap, especially in the self-consistent *GW* of 2.76 eV [39].

The computed biaxial band gap *tuning* for the K → K is depicted in Fig. 4(b). We extract *gauge factors* of 136 and 107 meV/% close to the zero strain point for the fixed-node QMC and DFT-PBE, respectively. Experimentally, the biaxial gauge factors are found 2.3 times the uniaxial strain ones [20], which would correspond to ≈60 (QMC) or 47 meV/% (DFT-PBE) uniaxial gauge factor. The gauge factors extracted from other treatments, see Table I, are surprisingly similar, suggesting that the different gaps respond to strain in a very similar manner. The experimental values for the uniaxial gauge factors for A and B excitons vary in a wide range of ≈(40–125) meV/% [19]; see Table I. Despite the wide strainability, most of the experiments use only subpercentage strains and the resulting gap tuning is of the order of a few hundredths of eV and they only cover the region of the K → K transition. It should also be noted that the experimental gauge factors are extracted from either photoluminiscence (PL) or optical absorption (OA), i.e., they correspond to optical gaps, whereas the computed gauge factors correspond to quasiparticle gaps. We presume that the wide spread of the experimental data is at least partly due to the substrate tuning, similarly to the situation with the experimental band gap value.

TABLE I. Calculated and experimental gauge factors. First line: Comparison of calculated QMC, *GW*, DFT-PBE, DFT-HSE, and DFT-B3LYP and experimental (PL, OA) gauge factors (in meV/% of applied strain) for the K → K transition. The first entry of the calculated values corresponds to the biaxial strain as directly calculated. The second entry is the value adjusted by a factor of 2.3, corresponding to the relation experimentally determined between biaxial- and uniaxial strains [20]. The experimental values is the data compiled from Refs. [17–20], which correspond to uniaxial strain. The *GW* results are from Ref. [28]. Last two lines: The calculated biaxial gauge factors for the Γ → K, and K → K/2 transitions. Note that no experimental values are available as the experiments have been limited to too small strain loads. All calculated data are based on quasiparticle band gap data close to the transition points (K → K–Γ → K and K → K–K → K/2), whereas all experimental data are based on optical band gaps as determined by PL and OA. No distinction is made between A and B excitons as the spin-orbit splitting is two small on the straintronics energy scale, see also Sec. III B.

	Gauge factor					
Transition	QMC	*GW*	PBE	HSE	B3LYP	exp
K → K	136/60	138/60	104/47	149	145	40–125
Γ → K	227	271	198	198	196	
K → K/2	42	83	40	41	41	

B. Boundaries between different band gap types

The different band gaps corresponding to different excitations have initially been pre-screened in the DFT-PBE model [33]. To outline the boundaries of the direct K → K band gap more accurately, we have performed fixed-node QMC calculation of the *boundaries* between the K → K and the Γ → K and K → K/2 due to applied strain and constructed the band-gap phase diagram; see Fig. 5. The band-gap gauge factors in those three areas (K → K, Γ → K, K → K/2) are determined as well; see Table I. The boundaries are determined from intersections between the corresponding parabolas for fitting parameters; see Appendix B. The boundaries in DFT-PBE and fixed-node QMC look qualitatively similar, the main difference being that all the DFT-PBE band gaps are almost rigidly reduced by ≈1 eV and the region of direct K → K-type band gap is smaller in the DFT-PBE model (2.79 vs. 2.03%). Our QMC calculation predicts the K → K direct band gap to be stable up to ≈0.51% tensile strain, which agrees very well with the experimental tuning in the tensile strain of up to ≈0.6% [17,19].

Inspection of Fig. 5 reveals that the SOCs, while rather small at the straintronics energy scale, do cause noticeable changes in the boundaries separating the different band-gap types. For instance, without the SOCs, the region of the direct K → K band-gap type would reduce by ≈0.6% and the boundary between the K → K and Γ → K band-gap type would coincide with zero strain and, hence, the above mentioned agreement with the straintronic experiments would be lost.

The direct K → K band gap in MoS_2 of ≈2.8% mostly in the compressive strain region is significantly smaller than that of the direct Γ → Γ band gap in phosphorene, which extends

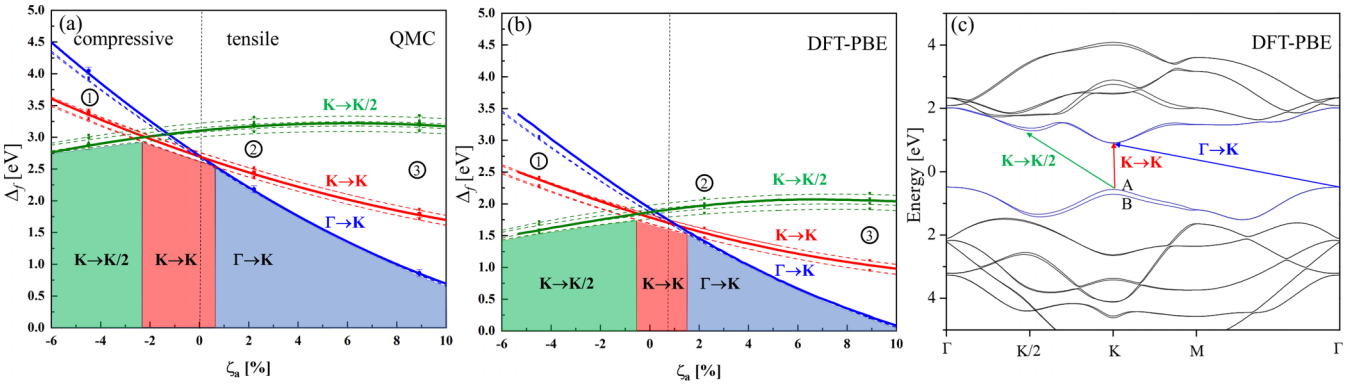

FIG. 5. Boundaries between K → K, Γ → K, and K → K/2. (a) The boundary between K → K, Γ → K, and K → K/2 as a function of applied biaxial strain as calculated in fixed-node QMC. (b) The same but for the DFT-PBE results. The dashed lines are the gaps with spin-orbit coupling corrections calculated in points 1–3 and fitted by quadratic formulas; see the main text. The zero strain (indicated by broken vertical lines in each description) is aligned to the fixed-node QMC value. (c) Illustration of the different band gap types, K → K, Γ → K, and K → K/2 in the full-relativistic DFT-PBE description corresponding to point 2. A and B label the A and B excitons; see the main text.

well over 10%, primarily into the tensile strain region, and is essentially only limited by the mechanical breakage of the material [22].

Inspection of the band-gap phase diagrams obtained by DFT-HSE, DFT-B3LYP hybrid functionals, and *GW* in Appendix A and QMC and DFT-PBE analyzed above strongly suggest that all of them are qualitatively similar. In particular, they all feature similar gauge factors and the curvatures of the lines separating the different excitations are also very similar, see Tables III and IV, meaning that the response of those excitations to strain is described with comparable accuracy in all treatments considered. What separates them are the values of the band gaps (vertical offsets), the relative values of the band gaps corresponding to the different excitations, and the equilibrium structures, see Sec. III C and Appendix A. As a result, the boundaries are shifted in an *ad hoc* manner compared to fixed-node QMC: In *GW* and DFT-B3LYP, the K → K bad gap cannot be tuned into the tensile region, while the opposite is true in DFT-HSE, which allows for significant tuning in the tensile strain and is very limited in the compressive strain. Overall, the DFT-PBE band-gap phase diagram appears most akin to the fixed-node QMC. In conclusion, only electronic structure methods simultaneously featuring ultra-accurate band gaps for *all* types of excitations and accurate equilibrium structures, such as fixed-node QMC, can provide faithful band-gap phase diagram.

C. Ground-state properties

Finally, we discuss the *deformation energies* (QMC, DFT-PBE, DFT-HSE, and DFT-B3LYP), Fig. 6; parameters of the paraboloid fits can be found in Appendix B. The deformation energies in all DFT descriptions are qualitatively similar to that of fixed-node QMCs. The main difference being the lattice constants which differ by +0.66%, −0.28%, and +2.25% from the fixed-node QMC for DFT-PBE, DFT-HSE, and DFT-B3LYP, respectively. As a result, the DFT-HSE functional provides the most accurate description of deformation energies. However, the DFT-HSE provides a band gap in equilibrium 0.45 eV too small and a band-gap phase diagram artificially exaggerating the strain tuning in the tensile region.

IV. CONCLUSION AND OUTLOOK

Using state-of-the-art QMC methods, we have determined straintronics functionalities of single-layer MoS_2. Based on this highly accurate many-body treatment, we predict the gauge factor of 136/59 meV/% for biaxial (uniaxial) strain, in line with the experimental values of ≈100 meV/% which, though, exhibit huge spreads. Such values of gauge factors are comparable to what we also determined for single-layer phosphorene [22]. We have also localized the excited state crossings between the direct K → K, Γ → K, and K → K/2 excitations under biaxial strain. In our QMC study, we have only studied three selected excitations, but applied strain will continuously affect the entire band structure and, hence, will affect the carrier effective mass. Strain may also affect the

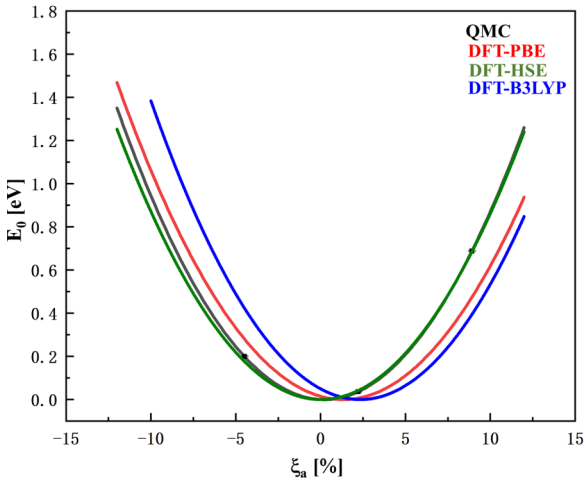

FIG. 6. Ground-state properties. Deformation energies in eV/unit cells, in fixed-node QMC, and in DFT- PBE, DFT-HSE, and DFT-B3LYP treatments.

TABLE II. Comparison of equilibrium properties in various treatments. Compared are equilibrium lattice constant a, quasiparticle band gap Δ_f, and SOC splitting at the K point in fixed-node QMC, *GW*, DFT-PBE, DFT-HSE, and DFT-B3LYP treatments. The first entry for the *GW* quasiparticle band gap corresponds to G_1W_0 [40] and the second entry to self-consistent *GW* [39]. Note that the SOC splitting added to fixed-node QMC is based on DFT-PBE.

Equilibrium data					
Method	QMC	*GW*	PBE	HSE	B3LYP
a (Å)	3.159±0.0006	3.18	3.18	3.15	3.23
Δ_f (eV)	2.69±0.051	2.84 2.76	1.69	2.24	2.38
SOC splitting (meV)	144	146	144	187	187

band structure in a discontinuous manner when the order of two bands with different curvatures is abruptly changed at a critical value of applied strain [22]. In MoS_2, the window where the direct $K \rightarrow K$ band gap is maintained is from -2.26% to 0% (compressive) and from 0 to 0.51% (tensile). Application of the strain in that interval changes the band gap merely by ≈0.3 eV. This is in line with experimental finding suggesting band gap modification by ≈0.05 eV due to applied tensile strain of ≈0.5% [16], in agreement with our fixed-node QMC model. This is smaller by an order of magnitude when compared to some other 2D materials, such as phosphorene [22], where both the applicable strain window and the quasiparticle gap modification maintaining the direct band gap are both significantly larger. This fairly limited straintronic functionality is surprising for a quintessential straintronic material for which most of the straintronic experiments have been performed [16].

Comparison of band-gap phase diagrams computed with different exchange-correlation functionals has revealed that a precise location of the excitation crossings requires ultra-accurate electronic and atomic structure treatments which describe, with high accuracy, all the band gaps (and form of the bands forming them) and their mutual relation in addition to correct equilibrium structure. Such requirements are *not* satisfied with most DFT functionals and, hence, they predict erratic results.

The same highly accurate QMC methodology could now be equally well applied to other 2D materials or to other tuning options, such as layer engineering, dielectric embedding, capping, or their combination. The latter factors are under poor experimental control and account for the huge differences in the measured properties. Hence, given the high accuracy of the QMC method, combined with the precise control of the system, the QMC-computed results may challenge the accuracy of the experimental results.

ACKNOWLEDGMENTS

Y.H., J.B., M.M., and I.S. were supported by APVV-21-0272, VEGA-2/0070/21, and I.S. also by VEGA-2/0131/23 projects. Y.H., J.B., and I.S. also acknowledge support from the H2020 TREX GA 952165 project. This project has received funding from the European Union's Horizon 2020 research and innovation program under the Programme SASPRO 2 COFUND Marie Sklodowska-Curie Grant Agreement No. 945478. Results of this research have been obtained using the resource Marconi100 at CINECA, Bologna, Italy, from the PRACE TIER0 Project No. 2021250026 *Novel Materials Properties Engineering via Pressure and Strain*. Part of the simulations were also performed on the Luxembourg national supercomputer MeluXina under the EuroHPC project HPC-REG-2022R03-222 *Quantum Monte Carlo layer engineering in 2D materials*. The authors gratefully acknowledge the LuxProvide teams for their expert support. We also acknowledge use of the DECI resource Snellius based in the Netherlands with support from the PRACE aisbl (Grant No. 17DECI0039 NANOREAL) and use of the MASAMUNE-IMR supercomputer system at CCMS/IMR, Tohoku University, Japan. For testing purposes this research used also resources of the Oak Ridge Leadership Computing Facility at the Oak Ridge National Laboratory, Project CPH141, which is supported by the Office of Science of the U.S. Department of Energy under Contract No. DE-AC05-00OR22725.

TABLE III. Parameters of strained gap and deformation energy fits. Fitted parameters of equation (B1) for $K \rightarrow K$, $\Gamma \rightarrow K$, and $K \rightarrow K/2$ transitions and for deformation energies in fixed-node QMC and DFT-PBE, DFT-HSE, and DFT-B3LYP treatments.

Band gap				
xc	Transition	c_0	c_1	c_2
QMC	$K \rightarrow K$	2.698	−13.220	32.186
	$\Gamma \rightarrow K$	2.710	−26.170	59.978
	$K \rightarrow K/2$	3.104	3.839	−31.480
PBE	$K \rightarrow K$	1.792	−11.511	32.945
	$\Gamma \rightarrow K$	1.935	−24.613	60.392
	$K \rightarrow K/2$	1.867	4.809	−28.798
HSE	$K \rightarrow K$	2.241	−13.648	37.341
	$\Gamma \rightarrow K$	2.422	−26.297	59.797
	$K \rightarrow K/2$	2.475	−3.976	−28.339
B3LYP	$K \rightarrow K$	2.670	−13.295	35.061
	$\Gamma \rightarrow K$	2.843	−25.856	57.593
	$K \rightarrow K/2$	2.896	3.891	−29.023
Deformation energy				
QMC		0.000	−0.375	90.674
PBE		0.015	−2.214	82.522
HSE		0.000	−0.049	86.609
B3LYP		0.050	−4.250	90.903

APPENDIX A: COMPARISON OF RESULTS FROM VARIOUS TREATMENTS

Here we compare our fixed-node QMC results to results of standard DFT and *GW* modeling, which reveal insights into the corresponding inaccuracies and therefore open a window for educated use of the rapid DFT approaches. The equilibrium parameters are collected in Table II. Comparison of the fixed-node QMC straintronic properties with the DFT-PBE which was used to fix the nodal hypersurfraces is in the main text, Figs. 4 and 5. Here we add comparisons with results of

TABLE IV. Parameters of fits of strained gap spin-orbit splittings. Fitted parameters of Eq. (B1) for spin-orbit band-gap splittings of K → K, Γ → K, and K → K/2 transitions in various descriptions. The entry for the QMC corresponds to spin-orbit couplings added perturbatively via DFT-PBE. In the other DFT treatments (HSE, B3LYP), the spin-orbit couplings are treated consistently at the given DFT exchange-correlation model.

		1			2			3			4		
xc	Spin band transition	c_0	c_1	c_2	c_0	c_1	c_2	c_0	c_1	c_2	c_0	c_1	c_2
	K → K	2.767	−12.759	28.037	2.761	−12.566	26.500	2.617	−12.834	27.965	2.623	−13.027	29.501
QMC and PBE	Γ → K	2.676	−25.086	49.106	2.670	−24.893	47.571						
	K → K/2	3.077	3.266	−26.909	3.149	3.084	−24.806	3.005	2.816	−23.341	3.221	3.534	−28.374
	K → K	2.761	−12.566	26.500	2.617	−12.834	27.965	2.623	−13.027	29.501	2.767	−12.759	28.037
PBE	Γ → K	2.670	−24.893	47.571	2.676	−25.086	49.106						
	K → K/2	3.149	3.084	−24.806	3.005	2.816	−23.341	3.221	3.534	−28.374	3.077	3.266	−26.909
	K → K	2.3218	−13.475	36.890	2.136	−13.864	37.804	2.337	−13.259	35.226	2.151	−13.647	36.140
HSE	Γ → K	2.401	−26.101	58.310	2.417	−25.885	56.646						
	K → K/2	2.520	3.887	−26.995	2.334	3.498	−26.081	2.611	4.385	−31.116	2.425	3.997	−30.202
	Γ → K	2.822	−25.674	56.084	2.839	−25.457	54.638						
	K → K/2	2.942	3.8040	−27.577	2.756	3.426	−26.729	3.032	4.28	−31/841	2.847	3.910	−30.993

hybrid DFT functionals (DFT-HSE and DFT-B3LYP) and results of *GW* modeling [28]. The comparison in Fig. 7 suggests an extreme sensitivity of the straintronic diagrams to both structural and electronic structure details. Inspection of Fig. 7 shows that while DFT-HSE artificially enlarges the region of the tensile strain, DFT-B3LYP reduces the region of tensile strain to zero and artificially enhances the region of compressive strain with respect to the fixed-node QMC. Similarly to DFT-B3LYP, *GW* also reduces the region of tensile strain to zero but has a narrower region of compressive strain than fixed-node QMC. Hence, taking into account all DFT and *GW* results, the DFT-PBE shows qualitatively the best agreement with fixed-node QMC, see Fig. 5.

APPENDIX B: STRAINED GAP, FIT PARAMETERS, AND EQUATIONS

From finite-size scaling, the infinite-size limits were extracted for three explicitly QMC calculated values (1–3, see Fig. 3) through which a quadratic form was fitted:

$$\Delta_f(a) = c_0 + c_1 \times a + c_2 \times a^2. \tag{B1}$$

The fitting parameters in formula Eq. (B1) are compiled in Table III. Quadratic fits were also used to fit the deformation energies, see Table III.

APPENDIX C: SPIN-ORBIT COUPLING CORRECTIONS

The fixed-node QMC calculations are performed without SOC taken into account. However, as is also well-known experimentally, the SOC is fairly weak but non-negligible in MoS_2 [16]. The effect of SOC was in the fixed-node QMC calculations applied *a posteriori* as a correction calculated at the DFT-PBE level. For that purpose, we have performed band-structure calculation for the MoS_2 monolayer along the Γ-K-M-Γ path using the QUANTUM ESPRESSO code again in DFT-PBE approximation and with a mesh of 20 × 20 k-points [41] for Brillouin zone integration. To assess the effect of SOC, two sets of calculations have been performed, a fully relativistic and scalar-relativistic with two sets of pseudopotentials, namely, fully relativistic (scalar relativistic) to calculate the electronic band structures with (without) the presence of the SOC.

To determine the spin-splitting parameters along the given path, the symmetry constraints have been taken into account.

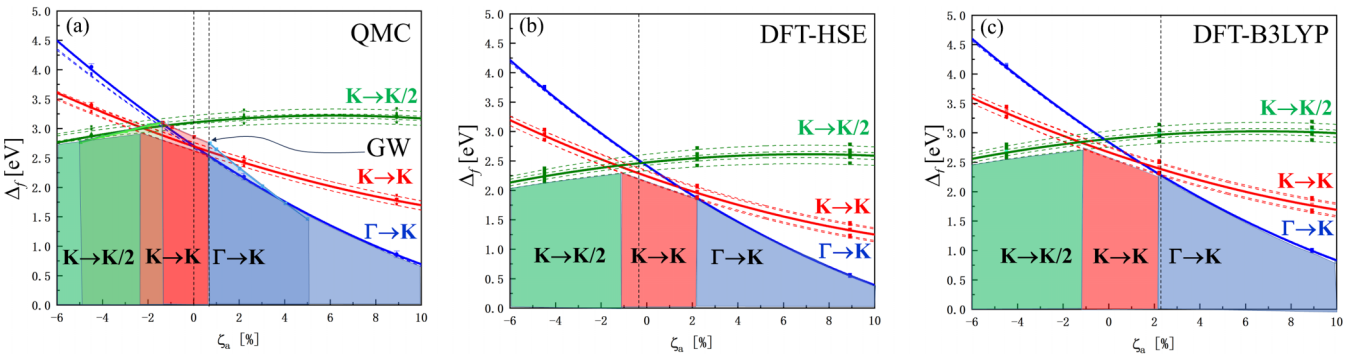

FIG. 7. Comparison of boundaries between K → K, Γ → K, and K → K/2 in various DFT and *GW* treatments. The diagrams are plotted against fixed-node QMC equilibrium. The respective *GW*, DFT-HSE, and DFT-B3LYP zero-strain states are indicated by dashed vertical lines.

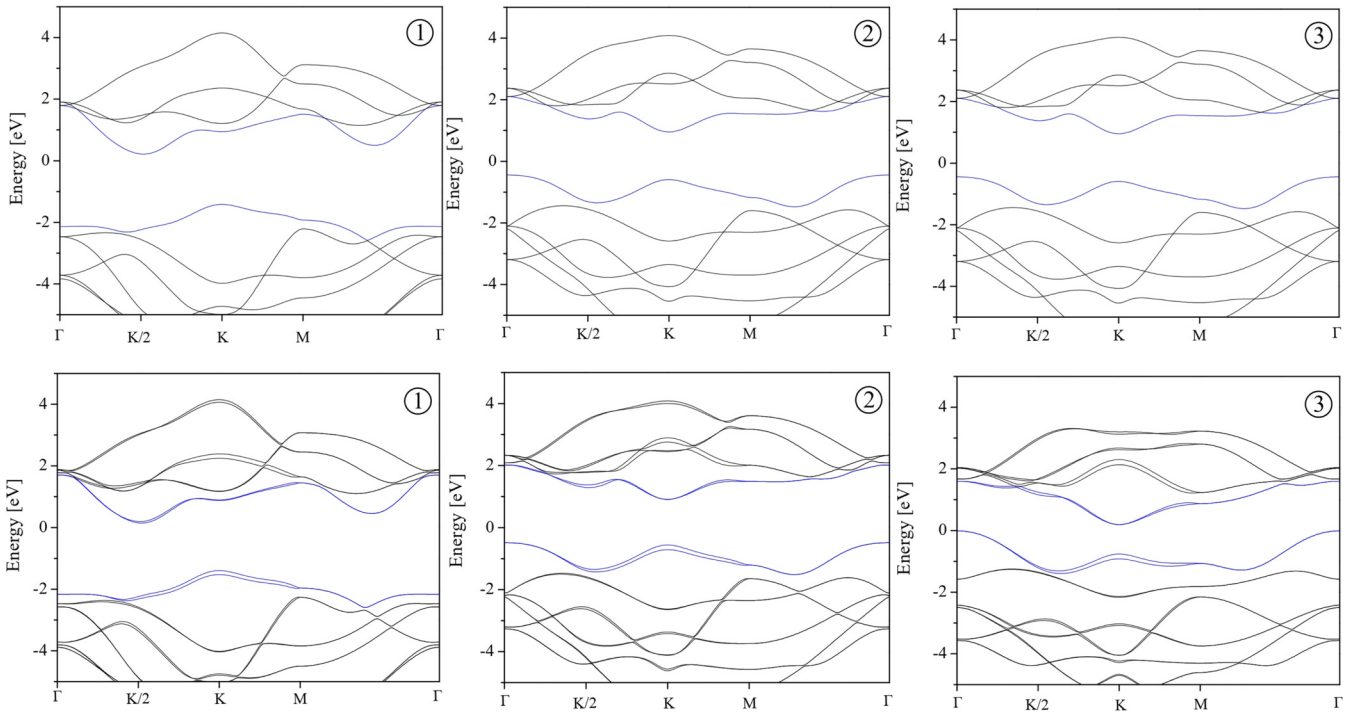

FIG. 8. SOC effects calculated with DFT-PBE exchange-correlation functional for three strained structures. Top panel: Results of scalar relativistic modeling; Bottom panel: Results of fully relativistic description. Calculations have been made for three different strain loads which were used in constructing the quadratic fits. For location of the points, refer to Fig. 5 in the main text.

Spin splitting of the bands was not allowed at the Γ point and along the M-Γ path. On the other hand, the spin splitting of the top valence band reaches the maximum value at the K point, while the maximum spin splitting of the lowest conduction band is located on the Γ-K path, close to the K/2 point. The calculations were performed at three different strains, labeled (1)–(3) in Fig. 8, which summarizes the results. For location of points (1)–(3), refer to Fig. 5 of the main text. In addition to DFT-PBE, fully relativistic DFT calculations were also performed with the DFT-HSE and DFT-B3LYP and used in constructing the DFT-HSE and DFT-B3LYP band-gap phase diagrams in Fig. 7. The effect of the exchange-correlation functional on the SOC splitting was found minute. The parameters of SOC corrections fitted with quadratic formulas Eq. (B1) are summarized in Table IV for all models considered.

The DFT-PBE spin splitting values of 130 meV, 151 meV, and 158 meV for the top valence band at the K point for the three structures of interest suggest that there is a moderate effect of strain on the spin-splitting value. The zero-strain reference is 148 meV [42]. For the bottom conduction band at the K point, we obtain the values 18 meV, 3 meV, and 1.5 meV (the spin-splitting value in the zero-strain case is 3 meV [43]). Finally, spin-splitting values of the bottom conduction at the K/2 point are 45 meV, 81 meV, and 85 meV.

[1] L. Li, Y. Yu, G. J. Ye, Q. Ge, X. Ou, H. Wu, D. Feng, X. H. Chen, and Y. Zhang, Black phosphorus field-effect transistors, Nat. Nanotechnol. **9**, 372 (2014).

[2] H. Liu, A. T. Neal, Z. Zhou, Z. Luo, X. Xu, D. Tomanek, and P. D. Ye, Phosphorene: An unexplored 2D semiconductor with a high hole mobility, ACS Nano **8**, 4033 (2014).

[3] K. Novoselov, A. Geim, S. Morozov, D. Jiang, Y. Zhang, S. Dubonos, I. Grigorieva, and A. Firsov, Electric field effect in atomically thin carbon films, Science **306**, 666 (2004).

[4] B. Hunt, J. D. Sanchez-Yamagishi, A. F. Young, M. Yankowitz, B. J. LeRoy, K. Watanabe, T. Taniguchi, P. Moon, M. Koshino, P. Jarillo-Herrero, and R. Ashoori, Massive Dirac fermions and Hofstadter butterfly in a van der Waals heterostructure, Science **340**, 1427 (2013).

[5] K. F. Mak, C. Lee, J. Hone, J. Shan, and T. F. Heinz, Atomically thin MoS_2: A new direct-gap semiconductor, Phys. Rev. Lett. **105**, 136805 (2010).

[6] K. Watanabe, T. Taniguchi, and K. Hisao, Direct-bandgap properties and evidence for ultraviolet lasing of hexagonal boron nitride single crystal, Nat. Mater. **3**, 404 (2004).

[7] W. Han, R. Kawakami, M. Gmitra, and J. Fabian, Graphene spintronics, Nat. Nanotechnol. **9**, 794 (2014).

[8] B. Radisavljevic, A. Radenovic, J. Brivio, V. Giacometti, and A. Kis, Single-layer MoS_2 transistors, Nat. Nanotechnol. **6**, 147 (2011).

[9] H. Lee, S.-W. Min, Y.-G. Chang, M. Park, T. Nam, H. Kim, J. Kim, S. Ryu, and S. Im, MoS_2 nanosheet phototransistors with thickness-modulated optical energy gap, Nano Lett. **12**, 3695 (2012).

[10] S. Yang, Y. Chen, and C. Jiang, Strain engineering of two-dimensional materials: Methods, properties, and applications, InfoMat. **3**, 397 (2021).

[11] R. Roldán, A. Castellanos-Gomez, E. Capelluti, F. Guinea, and F. Guinea, Strain engineering in semiconducting two-dimensional crystals, J. Phys.: Condens. Matter **27**, 313201 (2015).

[12] Z. Dai, L. Liu, and Z. Zhang, Strain engineering of 2D materials: Issues and opportunities at the interface, Adv. Mater. **31**, 1805417 (2019).

[13] C. Lee, X. Wei, J. Kysar, and J. Hone, Measurement of the elastic properties and intrinsic strength of monolayer graphene, Science **321**, 385 (2008).

[14] A. Bertolazzi, J. Brivio, and A. Kis, Stretching and breaking of ultrathin MoS_2, ACS Nano **5**, 9703 (2011).

[15] S. Thompson *et al.*, A 90-nm logic technology featuring strained-silicon, IEEE Trans. Electron Dev. **51**, 1790 (2004).

[16] R. Ganatra and Q. Zhang, Few-layer MoS_2: A promising layered semiconductor, ACS Nano **8**, 4074 (2014).

[17] K. He, C. Poole, K. Mak, and J. Shan, Experimental demonstration of continuous electronic structure tuning via strain in atomically thin MoS_2, Nano Lett. **13**, 2931 (2013).

[18] Y. Hui, X. Liu, W. Jie, N. Yui, N. Chan, J. Hao, Y.-T. Hsu, L.-J. Li, W. Guo, and S. P. Lau, Exceptional tunability of band energy in a compressively strained trilayer MoS_2 sheet, ACS Nano **7**, 7126 (2013).

[19] F. Carrascoso, H. Li, R. Frisenda, and A. Castellanos-Gomez, Strain engineering in single-, bi- and tri-layer MoS_2, $MoSe_2$, WS_2 and WSe_2, Nano Res. **14**, 1698 (2021).

[20] F. Carrascoso, R. Frisenda, and A. Castellanos-Gomez, Biaxial versus uniaxial strain tuning of single-layer MoS_2, Nano Mater. Sci. **4**, 44 (2022).

[21] W. M. C. Foulkes, L. Mitas, R. J. Needs, and G. Rajagopal, Quantum Monte Carlo simulations of solids, Rev. Mod. Phys. **73**, 33 (2001).

[22] Y. Huang, A. Faizan, M. Manzoor, J. Brndiar, L. Mitas, J. Fabian, and I. Štich, Colossal band gap response of single-layer phosphorene to strain predicted by quantum Monte Carlo, Phys. Rev. Res. **5**, 033223 (2023).

[23] T. Frank, R. Derian, K. Tokar, L. Mitas, J. Fabian, and I. Stich, Many-body quantum Monte Carlo study of 2D materials: Cohesion and band gap in single-layer phosphorene, Phys. Rev. X **9**, 011018 (2019).

[24] E. Gaufrés, F. Fossard, V. Gosselin, L. Sponza, F. Ducastelle, Z. Li, S. G. Louie, R. Martel, M. Côté, and A. Loiseau, Momentum-resolved dielectric response of free-standing mono, bi-, and trilayer black phosphorus, Nano Lett. **19**, 8303 (2019).

[25] E. Scalise, M. Houssa, G. Pourtois, V. V. Afanasév, and A. Stesmans, First-principles study of strained 2D MoS_2, Physica E **56**, 416 (2014).

[26] J. Petö, G. Dobrik, G. Kukucska, P. Vancsó, A. Koós, J. Koltai, P. Nemes-Incze, C. Hwang, and L. Tapasztó, Moderate strain induced indirect bandgap and conduction electrons in MoS_2 single layers, npj 2D Mater. Appl. **3**, 39 (2019).

[27] S. Postorino, D. Grassano, M. D'Alessandro, A. Pianetti, O. Pulci, and M. Palummo, Strain-induced effects on the electronic properties of 2D materials, Nanomater. Nanotechnol. **10**, 184798042090256 (2020).

[28] R. K. Defo, S. Fang, S. N. Shirodkar, G. A. Tritsaris, A. Dimoulas, and E. Kaxiras, Strain dependence of band gaps and exciton energies in pure and mixed transition-metal dichalcogenides, Phys. Rev. B **94**, 155310 (2016).

[29] M. Dubecký, F. Karlický, S. Minárik, and L. Mitas, Fundamental gap of fluorographene by many-body *GW* and fixed-node diffusion Monte Carlo methods, J. Phys. Chem. **153**, 184706 (2020).

[30] J. P. Perdew, K. Burke, and M. Ernzerhof, Generalized gradient approximation made simple, Phys. Rev. Lett. **77**, 3865 (1996).

[31] A. V. Krukau, O. A. Vydrov, A. F. Izmaylov, and G. E. Scuseria, Influence of the exchange screening parameter on the performance of screened hybrid functionals, J. Chem. Phys. **125**, 224106 (2006).

[32] P. J. Stephens, F. J. Delvin, C. F. Chabalowski, and M. J. Frisch, *Ab initio* calculation of vibrational absorption and circular dichroism spectra using density functional force fields, J. Phys. Chem. **98**, 11623 (1994).

[33] https://www.ui.sav.sk/w/wp-content/uploads/clanky/MoS2_gap_strained_SM.pdf.

[34] N. Alidoust, G. Bian, S.-Y. Xu, R. Sankar, M. Neupane, C. Liu, I. Belopolski, D.-X. Qu, J. D. Denlinger, F.-C. Chou, and M. Z. Hasan, Observation of monolayer valence band spin-orbit effect and induced quantum well states in MoX_2, Nat. Commun. **5**, 4673 (2014).

[35] A. Ambrosetti, F. Pederiva, E. Lipparini, and L. Mitas, Quantum Monte Carlo in presence of spin-orbit interaction, in *Advances in Quantum Monte Carlo*, edited by S. Tanaka, S. M. Rothstein, and W. A. Lester, Jr., ACS Symposium Series (2012), Vol. 1094, Chap. 10, pp. 119–130.

[36] J. Kim *et al.*, QMCPACK: an open source *ab initio* quantum Monte Carlo package for the electronic structure of atoms, molecules and solids, J. Phys.: Condens. Matter **30**, 195901 (2018), https://qmcpack.org/.

[37] P. Giannozzi, S. Baroni1, N. Bonini, M. Calandra, R. Car, C. Cavazzoni, D. Ceresoli, G. L. Chiarotti, M. Cococcioni, I. Dabo *et al.*, QUANTUM ESPRESSO: A modular and open-source software project for quantum simulations of materials, J. Phys.: Condens. Matter **21**, 395502 (2009), https://www.quantum-espresso.org/.

[38] J. Ryou, Y.-S. Kim, K. C. Santosh, and K. Cho, Monolayer MoS_2 bandgap modulation by dielectric environments and tunable bandgap transistors, Sci. Rep. **6**, 29184 (2016).

[39] T. Cheiwchanchamnangij and W. Lambrecht, Quasiparticle band structure calculation of monolayer, bilayer, and bulk MoS_2, Phys. Rev. B **85**, 205302 (2012).

[40] D. Y. Qiu, F. H. da Jornada, and S. G. Louie, Optical spectrum of MoS_2: Many-body effects and diversity of exciton states, Phys. Rev. Lett. **111**, 216805 (2013).

[41] H. J. Monkhorst and J. Pack, Special points for Brillouin-zone integrations, Phys. Rev. B **13**, 5188 (1976).

[42] Z. Y. Zhu, Y. C. Cheng, and U. U. Schwingenschlögl, Giant spin-orbit-induced spin splitting in two-dimensional transition-metal dichalcogenide semiconductors, Phys. Rev. B **84**, 153402 (2011).

[43] K. Kośmider, J. W. González, and J. Fernández-Rossier, Large spin splitting in the conduction band of transition metal dichalcogenide monolayers, Phys. Rev. B **88**, 245436 (2013).